PNAS RESEARCH ARTICLE | PHYSIOLOGY

Expression of H_v1 proton channels in myeloid-derived suppressor cells (MDSC) and its potential role in T cell regulation

Juan J. Alvear-Arias[a,b,1], Christian Carrillo[a,b,1], Javiera Paz Villar[a], Richard Garcia-Betancourt[a,2], Antonio Peña-Pichicoi[a,b], Audry Fernandez[a], Miguel Fernandez[a,b], Emerson M. Carmona[a,3], Amaury Pupo[a], Alan Neely[a], Osvaldo Alvarez[a,c], Jose Garate[a,b], Héctor Barajas-Martinez[d], H. Peter Larsson[e], Angélica Lopez-Rodriguez[f], Ramon Latorre[a], and Carlos Gonzalez[a,b,c,4]

Edited by Lily Jan, HHMI, University of California, San Francisco, CA; received March 6, 2021; accepted February 14, 2022

Myeloid-derived suppressor cells (MDSC) are a heterogeneous cell population with high immunosuppressive activity that proliferates in infections, inflammation, and tumor microenvironments. In tumors, MDSC exert immunosuppression mainly by producing reactive oxygen species (ROS), a process triggered by the NADPH oxidase 2 (NOX2) activity. NOX2 is functionally coupled with the H_v1 proton channel in certain immune cells to support sustained free-radical production. However, a functional expression of the H_v1 channel in MDSC has not yet been reported. Here, we demonstrate that mouse MDSC express functional H_v1 proton channel by immunofluorescence microscopy, flow cytometry, and Western blot, besides performing a biophysical characterization of its macroscopic currents via patch-clamp technique. Our results show that the immunosuppression by MDSC is conditional to their ability to decrease the proton concentration elevated by the NOX2 activity, rendering H_v1 a potential drug target for cancer treatment.

myeloid cells | H_v1 channel | immunosuppression | NOX2 complex | ROS

Significance

Immunosuppression by myeloid-derived suppressor cells (MDSC), especially near tumor surfaces, involves the extracellular production of reactive oxygen species (ROS). ROS generation in MDSC occurs during the oxidation of NADPH to NADP+, which NOX2 catalyzes. ROS react with the T cell receptor complex, abolishing the antigen presentation, which blocks the immune system elimination of the tumor cells. Extrusion of protons from MDSC by voltage-gated proton channel (H_v1) sustains ROS production. Here, we demonstrate the expression of H_v1 in mouse MDSC. In this way, H_v1 present in MDSC becomes a potential cancer therapeutic target since its inhibition seems to diminish immunosuppression activity in the tumoral microenvironment, allowing cancer cells to be attacked by the immune system.

Myeloid-derived suppressor cells (MDSC) are a heterogeneous myeloid cell population that appear in the final stages of inflammation and, as the name suggests, have powerful immunosuppressive activity (1). MDSC correspond to an intermediate stage of dendritic cell and macrophage differentiation during myelopoiesis (2), which spans from a proinflammatory to a strongly antiinflammatory process. The criteria to identify MDSC from the other myeloid-derived cellular lineages are still a matter of controversy (3). Notwithstanding, in mice MDSC are mainly characterized by the coexpression of Gr-1 and CD11b markers (4–6) and further differentiated into subtypes based on Gr-1 expression levels. These two MDSC subpopulations are grouped into the highly immunosuppressive mononuclear-MDSC (MO-MDSC) characterized by a lower expression of Gr-1 and the moderately immunosuppressive polymorphonuclear-MDSC (PMN-MDSC) with a higher Gr-1 expression (7). However, it is the ability to suppress both the proliferation and activation of T lymphocytes (T cells) that defines the MDSC (5, 6, 8, 10). This MDSC hallmark is what ultimately attracted the attention of the scientific community, due to its potential application to cancer therapy (1, 7, 8, 9, 11–14). Cancer cells have several mechanisms to become practically "invisible" to the immune system, and one of these strategies consists of the recruitment of MDSC within the tumoral microenvironment (11, 12). Once recruited, MDSC engage in the suppression of T cell proliferation through several mechanisms that include: 1) depleting the tumoral microenvironment of cysteine (13), 2) secreting arginase and interleukin 10 (9, 13–15), and 3) extracellular production of reactive oxygen species (ROS) (16, 17). The synergy of all these mechanisms results in a powerful and efficient suppression system. It is of importance for this work that ROS production affects the structure of T cell receptors (TCR) expressed in $CD8^+$ and $CD4^+$ lymphocytes membrane, rendering a suppressive function (13).

Antigen-presenting cells, like dendritic cells, can internalize tumor-associated antigens and process them into short peptides to be loaded onto the major histocompatibility complex (MHC) on their cellular surfaces (4). Usually, extracellular antigen presentation involves the protein MHC II, which in turn activates the $CD4^+$ T_{helper}-mediated cascade of humoral response. By contrast, the presentation of intracellular antigens uses MHC I and promotes the activation of $CD8^+$ cytotoxic cells. As the tumoral cells are not able to activate a sufficient response from $CD8^+$ cells, in order to elicit an immune response a cross-presentation must occur. This consists of dendritic cells acquiring tumoral-associated antigens from dying cells via micropinocytosis, endocytosis, or phagocytosis

The authors declare no competing interest.

This article is a PNAS Direct Submission.

[1]J.J.A.-A. and C.C. contributed equally to this work.

[2]Present address: Millennium Institute on Immunology and Immunotherapy, Programa de Inmunología, Instituto de Ciencias Biomédicas, Facultad de Medicina, Universidad de Chile, Santiago 8380453, Chile.

[3]Present address: Cell Physiology and Molecular Biophysics, Texas Tech University Health Sciences Center, Lubbock, TX 79430.

[4]To whom correspondence may be addressed. Email: carlos.gonzalezl@uv.cl.

This article contains supporting information online at http://www.pnas.org/lookup/suppl/doi:10.1073/pnas.2104453119/-/DCSupplemental.

Published April 4, 2022.

and loading them onto MHC I and subsequentially presenting these antigens to $CD8^+$ cells (18). Another way that the response can be initiated is by internalizing materials and membranes from living tumor cells by the antigen presenters. Cancer cells express aberrant proteins that can be recognized as antigens due to the multiple mutations suffered by the rapidly proliferating cells. This is known as the tumoral mutational burden (19). In this manner, the antigen-presenting cells can activate the $CD4^+$ via immune response by interfacing with the TCR. The presence of MDSC in this stage interrupts the immune response activation (20).

Sustained ROS production is required for the function of MDSC by the NADPH oxidase 2 complex (NOX2). In this process, NOX2 catalyzes the superoxide (O_2^-) production, a major ROS and a precursor of other ROS, by electron transfer from the NADPH coenzyme. Accordingly, this redox reaction produces H^+ during each enzymatic cycle, thus acidifying the cytosol (21). As acidic pH and membrane depolarization abolish the NOX2 activity (22, 23), it is impossible to achieve sustained ROS production without a regulatory mechanism of the intracellular pH (pH_i), membrane potential, and ion channels. The voltage-gated proton channel carries out the dissipation of these gradients by the extrusion of protons in other immune cells (H_v1). Many reports in the literature involve H_v1 activity in the context of immune responses, such as the respiratory bursts in phagocytosis (24–26).

The H_v1 proton channel is a 64-kDa homodimeric membrane protein. Each subunit encompasses four transmembrane segments (S1–S4) and one intracellular (S0), with intracellular C- and N-terminal (27, 28). The biophysical properties of the H_v1 macroscopic currents allow us to differentiate it from other ion channels. H_v1 currents (I_{H+}) are H^+-selective and highly sensitive to both the membrane potential and pH gradient ($\Delta pH = pH_o - pH_i$) across the membrane (29). The unitary conductance of H_v1 has been estimated in the order of femtosiemens, which is ∼1,000-fold smaller than the unitary conductance of *Shaker* potassium channels (30). H_v1 is strongly inhibited by Zn^{2+} and derivatives of 2-guanidinobenzimidazole (31, 32). These distinctive properties allowed for the identification of the H_v1 physiological role in proinflammatory immune system cells such as eosinophils, macrophages, and dendritic cells.

It has been widely reported that proper function of H_v1 supports the sustained ROS production via functional coupling with NOX2 complex, establishing positive feedback between both entities on myeloid-derived lineages (24–26). This trait of NOX2-mediated ROS production is also present in the antiinflammatory MDSC (33–35). However, the protein responsible for maintaining the intracellular pH and membrane potential during the immunosuppressive mechanism via ROS in MDSC is unknown. In the present study, we isolated and characterized MDSC from primary cultures of murine bone marrow and detected the presence of functional H_v1 channels. Then, we demonstrated that the H_v1 inhibition reduced the ROS production in MDSC and, in addition, this inhibition dramatically reduced its suppressive activity. Our results strongly suggest that H_v1 plays a crucial role in the immunosuppressive activity of MDSC and may provide a potential pharmacological target for cancer therapies.

Results

Cell Cultures Have the Characteristic Phenotype and Immunosuppressive Activity of MDSC. Myeloid precursors (MP) extracted from mouse bone marrow were cultured in the presence of granulocyte-macrophage colony-stimulating factor (GM-CSF). Nonpermeabilized cells were stained with the MDSC lineage markers CD11b and Gr-1 antibodies and subsequently analyzed by flow cytometry. Cells were selected by their morphology (side scatter versus forward scatter), and live cells were selected with the viability dye FVS-660 (*SI Appendix*, Fig. S1*A*). The expression of CD11b and Gr-1 was analyzed to estimate the cell percentage corresponding to MDSC in the cell culture (Fig. 1*A*, *Upper* and *SI Appendix*, Fig. S1*A*, *Right*). Since MDSC are an immature myeloid lineage that can differentiate into dendritic cells and macrophages, we screened cells according to the expression of MDSC markers Gr-1 and F4/80 that signal macrophage differentiation. We monitored the expression of the markers during a week of incubation in the presence of GM-CSF, to determine the best time frame in which to gather MDSC. Since the beginning of the experiment, the MDSC markers have increased steadily, while Gr-1 expression decreased in synchrony with an F4/80 expression increment (*SI Appendix*, Fig. S1*B*). Our results allowed us to determine that 96 h of culture is the best MDSC harvesting time when the presence of other myeloid lineages in the cultures is minimized (*SI Appendix*, Fig. S1*B*). Interestingly, our proliferation assays on MDSC cultures harvested show a significant ($P < 0.005$) evidenced immunosuppressive activity (*SI Appendix*, Fig. S2 *A* and *B*).

H_v1 Proton Channel Expression in MDSC. To assess whether H_v1 is expressed on these cells, MDSC and MP directly extracted from mouse bone marrow were lysed and analyzed by Western blot using an anti-H_v1 antibody. Our results show the presence of a ∼30-kDa protein band in the MDSC lane and a weak signal in the MP lane (Fig. 1*B* and *SI Appendix*, Fig. S3), corresponding to H_v1 monomers. In addition, to complete this finding we performed a flow cytometry assay, where we timed H_v1 expression while cell differentiation occurred. Several cultures of MDSC were monitored over the four differentiation days in the presence of GM-CSF and screened for H_v1 expression (*SI Appendix*, Fig. S4 *A* and *B*). Briefly, H_v1 presented a relatively low expression during the first days of culture but had a large expression spike near 96 h of differentiation. Thus, our results show that nearly all $CD11b^+/Gr\text{-}1^+$ cells were also positive for H_v1.

Functional H_v1 Proton Channels in MDSC Membranes. The whole-cell patch-clamp technique was performed to assess the H_v1 functional channel protein expression in primary cultures containing about 75 to 90% MDSC (*SI Appendix*, Fig. S1*A*, *Right*). Therefore, to carry out these electrophysiological assays, we identified MDSC from other cells by comparing their biochemical characteristics to a morphological one (Fig. 1*C*). As seen in the expression kinetics experiments (*SI Appendix*, Fig. S1*B*), opposite to CD11b, the Gr-1 marker decreased drastically until extinction after the fourth day of culture. Therefore, based on this biochemical criterion that allows us to differentiate the MDSC from their later stages, the $Gr\text{-}1^+$ cells' morphology was compared to $Gr\text{-}1^-$ cells by confocal microscopy. As Fig. 1*C* shows, $Gr\text{-}1^+$ cells are characterized by a small, round and non- or semiadherent phenotype (Fig. 1*C*, *Upper*). In contrast, cells that lack the Gr-1 marker possess an irregular, adherent phenotype, and some of them have cytoplasmic projections (Fig. 1*C*, *Lower*). Once the morphology of the $Gr\text{-}1^+$ cells was identified, the biophysical characterization of H_v1 channels was performed using patch clamp in whole-cell configuration (Fig. 2*A* *Middle* and *Left*, protocols inserted). These

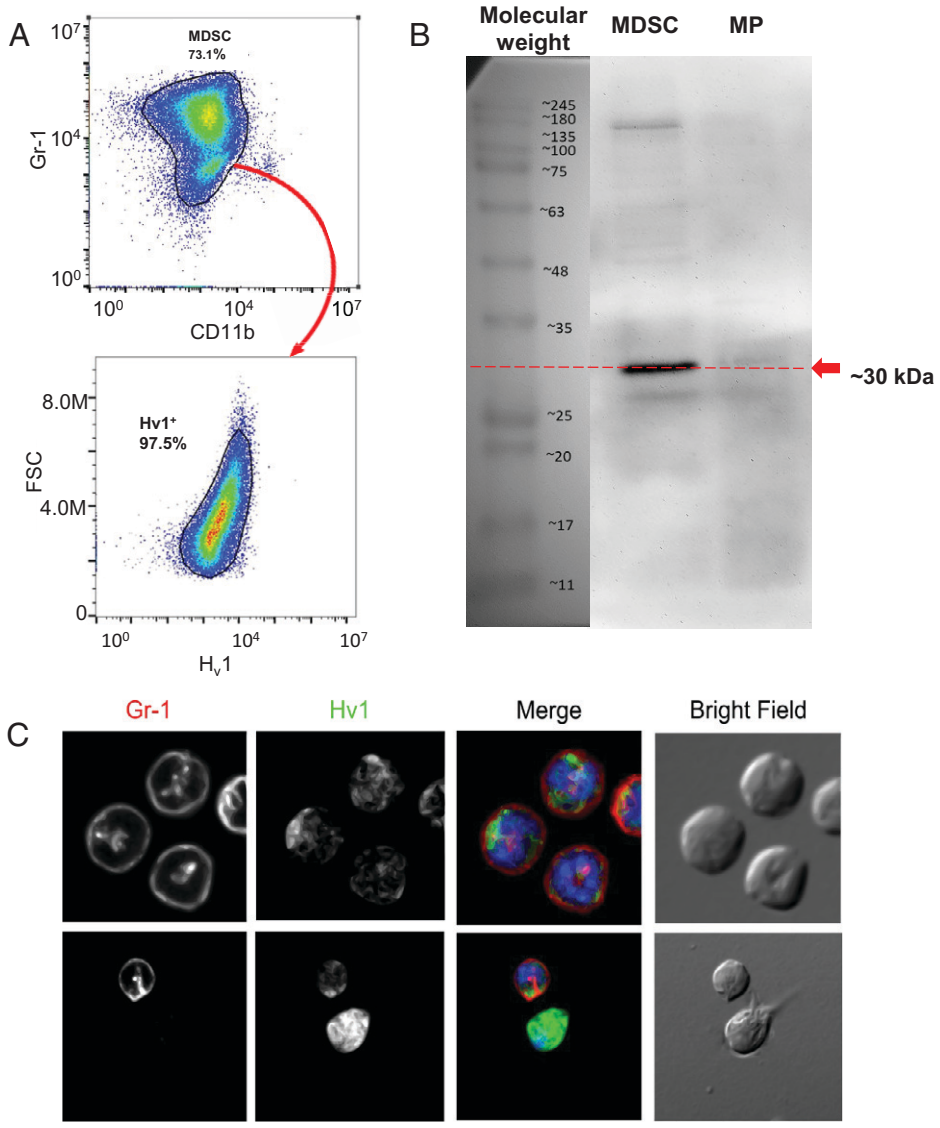

Fig. 1. H_v1 channel is expressed in mouse MDSC. Ninety-six hours after seeding bone marrow cells in the presence of GM-CSF, cell cultures were biochemically and morphologically analyzed. (*A*) H_v1 immunodetection by flow cytometry. A representative pseudocolor dot plot obtained by flow cytometry showed 73.1% of MDSC differentiated cells, indicating the expression of Gr-1 and CD11b markers; 97% of these immunostained cells are positive for Hv1 channels. (*B*) H_v1 immunodetection in MDSC cultures and MP. A band around 30 kDa corresponding to the predicted molecular weight for H_v1 monomers SDS-PAGE was evidenced by Western blot clearly in MDSC cultures, and in a highly diminished proportion also present in MP cultures. (*C*) Morphological characterization of Gr-1$^+$ cells. Morphological analysis was done corelating cell morphology with Gr-1 (in red) and H_v1 (in green) immunostaining. The Merge column shows H_v1 channel in MDSC differentiated cells expressing Gr-1 protein; the cell nucleus was marked with DAPI (in blue) for reference. The upper lane panels show four representative round and nonadherent cells, characterized as suppressor myeloid cells. The lower lane panels show morphological differences between myeloid and dendritic phenotypes illustrating that myeloid cells were rounded. Arrows are pointing to a myeloid cell.

ionic currents decreased at longer pulses and increased at more positive potential upon depolarization (Fig. 2*A*, *Middle*). Furthermore, we observed the appearance of inward tail currents at the holding potential (−90 mV) that is quite far from the equilibrium potential for protons (E_{H+}) in theoretical conditions (E_{H+}= −116 mV for ΔpH = 2). Both the decrease in proton currents and a more positive reversal potential than E_{H+} are due to H^+ depletion (36), which affects the proton currents due to the rapid change in pH in the vicinity of each channel. The effects mentioned above must be taken into account when interpretating the data. For this reason, the pulse protocol was optimized by decreasing the duration of the depolarizing pulses. This optimized voltage protocol produced stable macroscopic current traces with no inward tail currents corresponding to the proton gradient used (Fig. 2*A*, *Right*). The MDSC proton currents can be studied using this voltage protocol to study the ΔpH dependency of H_v1 channels.

MDSC Proton Currents Are Produced by H_v1. A hallmark of H_v1 currents is the dependence of the conductance-voltage (G-V) curves on the pH gradient ($\Delta pH = pH_o - pH_i$). Thus, to confirm that these proton currents arise from the H_v1 activity, we studied the ΔpH sensitivity of the MDSC G-V curves (Fig. 2 *B* and *C*). Using a ΔpH of 0, 1, and 2, we found that the H_v1 G-V curves were shifted toward the left along the voltage axis as the ΔpH increases (Fig. 2*C*). Moreover, activation time constants (τ_{act}) obtained by fitting the activation currents to a single exponential function become faster at more depolarizing voltages and higher ΔpH (*SI Appendix*, Fig. S5*A*). To evaluate if MDSC currents are proton-selective, the E_r was determined employing a fast ramp pulse protocol at several ΔpH values and compared with the analytical result from the Nernst equation (Fig. 2*D* and *SI Appendix*, Fig. S5 *B–D*). Showing that the recorded MDSC currents are proton-selective, the line described using a linear fit to the data has a

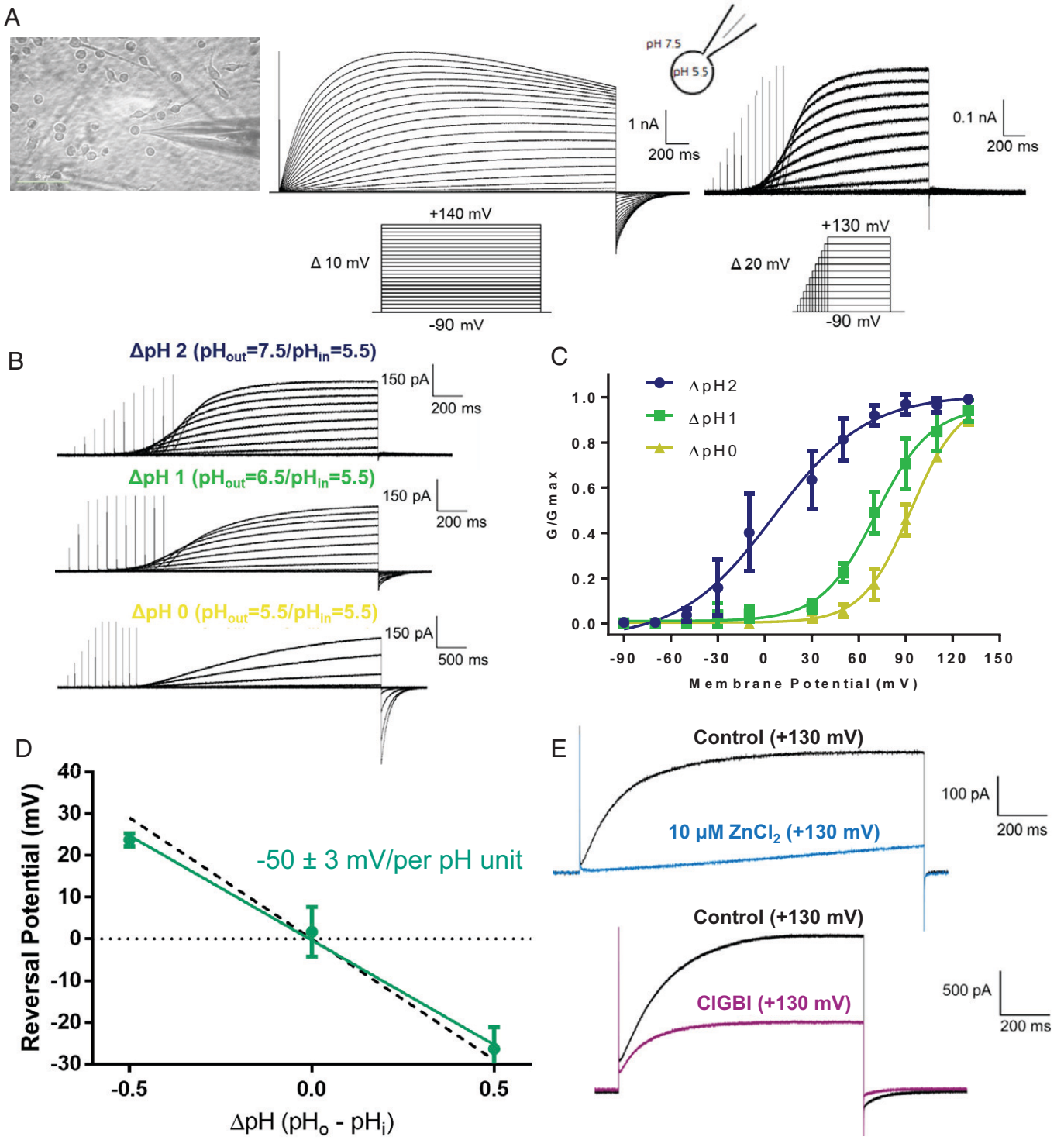

Fig. 2. Electrophysiological characterization of proton currents in MDSC. (*A*) Representative H+ currents in membrane patches from MDSC. Micrography showing how Gr-1+ morphology was used for selecting cells to perform electrophysiological measurements (*Left*). MDSC proton currents from selected cells were elicited with voltage pulses of 3 s in the range from −90 to +140 mV in 10-mV increments. Currents show proton depletion (*Middle*). Currents were obtained at ΔpH 2 by applying voltage pulses of variable duration, from a holding potential of −90 mV to +130 mV in increments of 20 mV to avoid depletion (*Right*). (*B* and *C*) ΔpH dependence of H_v1 channel on MDSC. (*B*) Representative currents were obtained at the different ΔpH conditions, pH 5.5 in the pipette solution (pHi) and various pH values in the bath solution (pHo) (5.5, 6.5, 7.5; $n = 4, 3, 3$, respectively), applying the optimized variable duration pulse protocol. Note that the pulse protocols applied to lower ΔpH records had a longer duration to allow for channel activation. (*C*) Normalized GV curves are shown at ΔpH 2 (5.6 ± 4 mV, $n = 4$), ΔpH 1 (71.08 ± 1.7 mV, $n = 3$), and ΔpH 0 (93.24 ± 1.4 mV., $n = 3$). Data were fitted by a Boltzmann function. (*D*) Proton selectivity of MDSC currents. Selectivity of voltage-gated proton currents in MDSC was estimated from reversal potential at different ΔpH. Representative current traces at different ΔpH −0.5, 0, and 0.5 ($n = 5, 5, 5$, respectively) were elicited using a fast ramp pulse protocol to determine the reversal potential of voltage-gated proton currents in MDSC. Er and ΔpH relationship is shown. The experimental values were fitted by a linear regression with a −50 mV per pH unit slope. The dashed line is the theoretical value predicted for protons by the Nernst equation (−58 mV per pH unit slope). (*E*) MDSC proton current inhibition. Representative current traces were elicited upon depolarization from −90 to +130 mV on a cell, before (black traces) and after inhibition (blue or purple traces). (*Top*) Representative traces after the inhibition induced by 4-min perfusion with 10 μM ZnCl2 (blue trace). (*Bottom*) Current traces corresponding to a cell, perfused for 1 min with 100 μM ClGBI (purple trace).

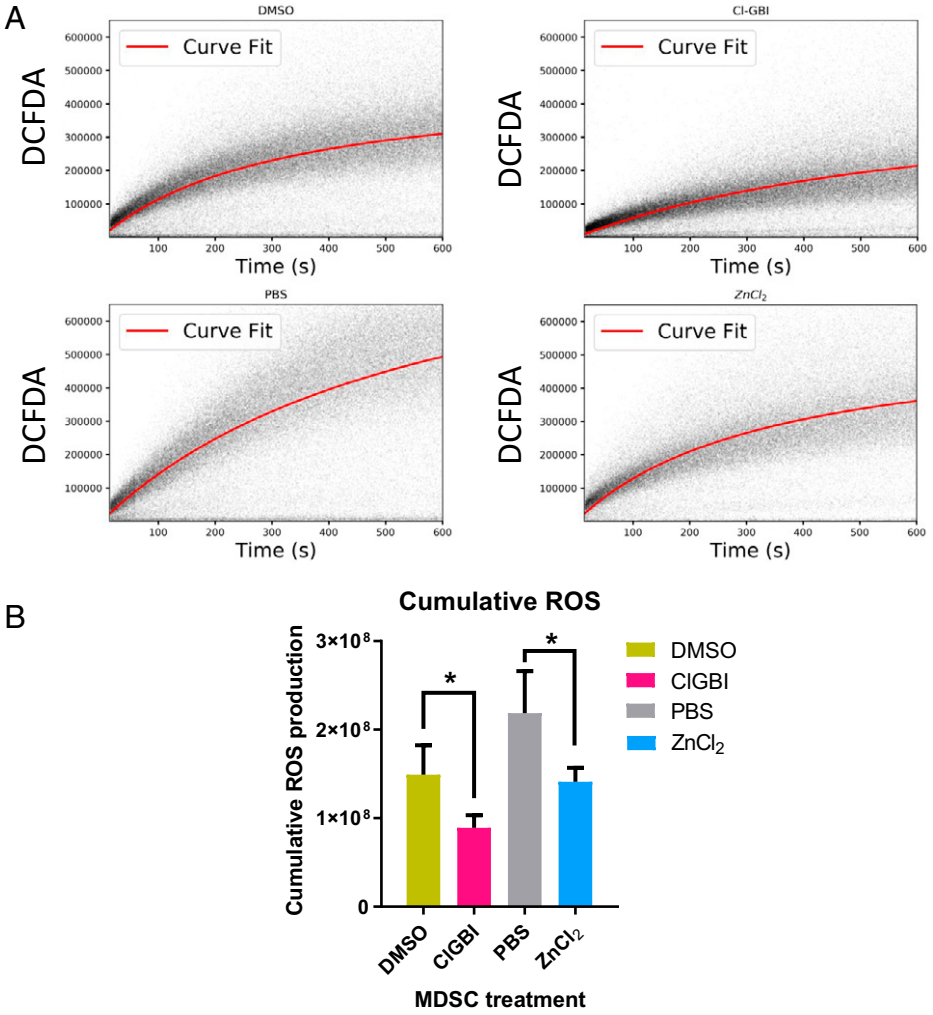

Fig. 3. Flow cytometry measurement of MDSC ROS production in the presence of H_v1 proton channel inhibitors. MDSC reactive species production was stimulated using 100 nM PMA. Changes in dichlorofluorescein fluorescence intensity (DCFDA), induced by the inhibitors used, 200 μM ClGBI, 1 mM $ZnCl_2$, or their respective vehicle controls (PBS or DMSO), were monitored for 10 min. (*A*) The detection of ROS production was fitted to the best curve possible via Python (red line) to better detect changes induced by the inhibitors or their respective vehicles. (*B*) The bar graph illustrates mean and SEM from the integrated curves for each condition, representing the cumulative ROS production. Asterisks indicate significative differences with $*P < 0.005$, according to nonparametric Kruskal–Wallis test. $n = 3$.

slope of −50 mV/ΔpH that slightly differs from the −58 mV/ΔpH predicted by the Nernst equation for a pH electrode. Finally, the application of 10 μM $ZnCl_2$ and 100 μM of the membrane-permeable H_v1 inhibitor 5-chloro-2-guanidinobenzimidazole (ClGBI) to the bath solution strongly inhibited MDSC proton currents (Fig. 2*E*). Together, these results indicate that the H_v1 channel is functionally expressed in MDSC; its biophysical fingerprints, including ΔpH gating, proton selectivity, and pharmacological inhibition by Zn^{2+} and ClGBI, indicate that this protein corresponds to the previously reported H_v1 channel in other mammalian cells (37).

H_v1 Modulation Alters ROS Production in MDSC. Since Hv1 is functionally expressed, we wondered if this channel can potentially involve proton extrusion in the immunosuppressive activity of MDSC. The functional coupling between H_v1 and the NOX2 complex in MDSC was assessed by flow cytometry comparing NOX2 activity in the presence and absence of H_v1 inhibitors, $ZnCl_2$ and ClGBI. The ROS-sensitive probe H_2DCFDA was used to track ROS generation after stimulating its production by using 100 nM phorbol 12-myristate 13-acetate (PMA), a well-known NOX2 activator (*SI Appendix*, Fig. S6). Fig. 3*A* shows representative results obtained for each different condition. The change in the fluorescence intensity of the H_2DCFDA probe was timed for 10 min, with recordings starting (t = 0) just after PMA stimulation (Fig. 3*A*). Each point corresponds to a single cell fluorescence recording. Fig. 3*B* summarizes three independent experiments. Like those shown in Fig. 3*A*, cumulative ROS produced was calculated as the mean of the integration value of the area below the curve for each experimental condition. Overall, cells incubated with $ZnCl_2$ or ClGBI presented a decrease in ROS production with respect to the control condition. The effect of inhibition by Zn^{2+} and 2-GBI produces a significant reduction of ROS production by MDSC when compared to the vehicles. This inhibition found in our experiments suggests that the H_v1 activity is required to sustain a high production of ROS in MDSC, pointing to a functional coupling between NOX2 and H_v1 in these immunosuppressive cells. Interestingly, we observed that after a 2-h incubation with the Hv1 inhibitors, ROS production decreased, and this decrement remained although inhibitors were washed out (*SI Appendix*, Fig. S11*A*). Moreover, this

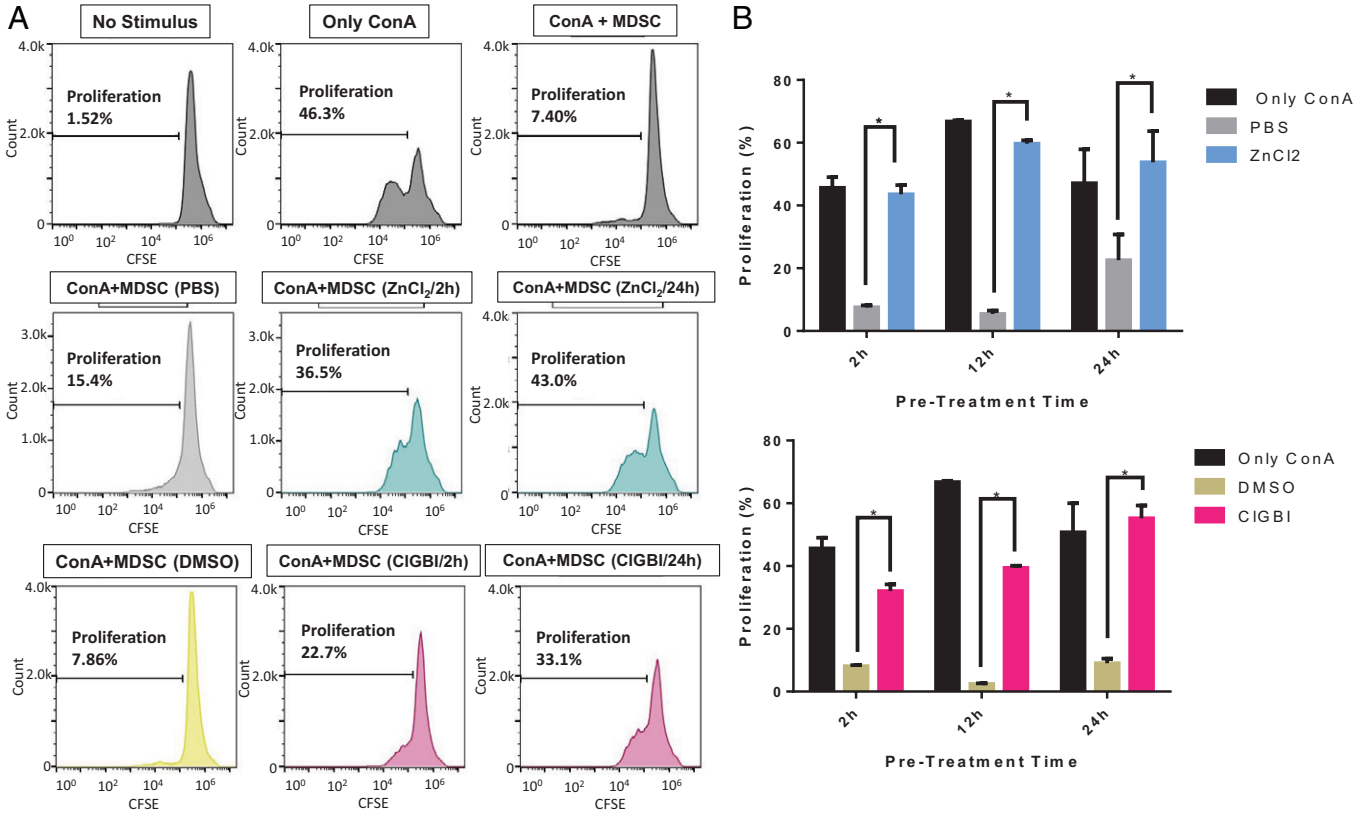

Fig. 4. Pretreatment of MDSC with H_v1 proton channel inhibitors diminish their capability to suppress mitogen-induced T cell proliferation. MDSC differentiated in vitro from bone marrow precursors of C57BL/6 mice were treated for 2, 12, and 24 h with 1 mM $ZnCl_2$ or with 200 μM ClGBI. Untreated cells, or cells treated with the ClGBI vehicle, DMSO, were used as a control. The ability of the MDSC to suppress T cell proliferation was assessed by stimulating CFSE-stained T cells with 2 μg/mL of ConA and culturing them for 96 h in the absence or presence of MDSC in ~1:10 of the splenocytes. (*A*) T cells proliferation assay. Representative histograms from flow cytometry analysis indicating the percentage of T cell proliferation for each experiment, T cell culture untreated (No Stimulus), T cells stimulated with ConA (Only ConA), stimulated T cell cocultured with MDSC (ConA + MDSC), stimulated T cells cocultured with MDSC pretreated for 2 or 24 h with $ZnCl_2$ [ConA + MDSC ($ZnCl_2$/2h)], and ConA + MDSC ($ZnCl_2$/24h), respectively, and the vehicle for the $ZnCl_2$ PBS [ConA + MDSC (PBS)]. The ClGBI vehicle was also used to induce cell proliferation, mixing with ConA + MDSC (DMSO), with ClGBI [ConA + MDSC (ClGBI/2h], or ConA + MDSC (ClGBI/24h). (*B*) Quantification of proliferation assay. T cell proliferation was calculated in the presence or absence of MDSC treated with ZnCl2 (*Top*) or ClGBI (*Bottom*) for 2, 12, and 24 h for three independent experiments. Proliferation comparison was done by graphing the Mean ± SE mean for each condition. Asterisks indicate significant differences *$P < 0.005$, by Kruskal–Wallis test.

effect seems to be irreversible even after 24-h removal of ClGBI, as recordings of MDSC still showed a stunted ROS production profile (*SI Appendix*, Fig. S11*B*).

H_v1 Blockers Abolish the Immunosuppressive Phenotype of MDSC. To test the immunosuppressor function of MDSC, a sine qua non feature of this cell population, we analyzed their ability to suppress the proliferation of T cells obtained from mouse spleen when stimulated by the addition of the mitogen Concanavalin A (ConA). When the T cells in cultures labeled with carboxyfluoresce in succinimidyl ester (CFSE) are stimulated and proliferate, the flow cytometer detects several peaks of green fluorescence in different fluorescent intensities. On the other hand, the appearance of a single, monodispersed peak on the CFSE histogram suggests that no mitosis took place, i.e., cells do not proliferate (*SI Appendix*, Fig. S7). As expected, the CFSE-labeled T cells gave rise to several proliferation peaks when stimulated by ConA. However, despite the ConA stimulus, little proliferation was encountered when cocultured with MDSC (*SI Appendix*, Fig. S2 *A* and *B*). Because ROS production, mainly by NOX2 in the MDSC, is key to this suppression, we tested the role of H_v1 in modulating this response. T cell proliferation was monitored in the presence of MDSC that were preincubated for 2, 12, and 24 h in 1 mM $ZnCl_2$ or 200 µM ClGBI solutions, respectively. MDSC ability to suppress T cell proliferation was assessed by stimulating CFSE-stained mice T cells stimulated with 2 µg/mL of ConA and cultured for 96 h, in the absence or presence of MDSC (*SI Appendix*, Fig. S8). MDSC cocultured in different ratios to T cells (1:5, 1:10, or 1:20) presented similar responses (*SI Appendix*, Fig. S10 *A* and *B*). Thus, the concentration of MDSC has little influence on their suppressor activity. A ratio of 1 MDSC per 10 T cells (1:10) was therefore used in all remaining experiments.

One major concern involves a decrease of cell viability due to increased cytosolic acidity caused by H_v1 inhibition, which would also result in cell proliferation. Briefly, our results show that long exposures (12 and 24 h) to H_v1 inhibitors are harmful to MDSC. Accordingly, cell viability was measured by FVS-660 (*SI Appendix*, Fig. S10 *C* and *D*), which decreases by 50% when cells are incubated for 24 h in the presence of the inhibitor. However, the survival of MDSC after 2 h of incubation with the H_v1 inhibitors is comparable to control conditions (*SI Appendix*, Fig. S10 *C* and *D*). In general, MDSC treated with the inhibitors could not suppress proliferation as compared to control conditions (Fig. 4*A*). The presence of MDSC abolished T cell proliferation, but this situation is reversed when MDSC were pretreated by Zn^{2+} (Fig. 4*A*, *Middle*) or ClGBI (Fig. 4*A*, *Bottom*). Both inhibitors recover proliferation when MDSC are treated for at least 2 h and recovery is essentially complete with a 12-h pretreatment (Fig. 4*B*). These results clearly show that

by modulating H_v1 channel activity the suppressive function of MDSC is reduced. Consequently, the decrease of the immunosuppressor capabilities observed after 2-h preincubation seems related to the previously detected ROS decrement (*SI Appendix*, Fig. S11). As the phenotypic change to a lesser immunosuppressive and lesser ROS-producing cell might be related to a change in cell identity, we analyzed the MDSC expression markers after preincubation. As shown in *SI Appendix*, Fig. S13, 2-h incubation is enough to induce a fluorescent intensity shift for both CD11b and Gr-1, suggesting a change in the ratio of MDSC subpopulations (MO- and PMN-MDSC).

Discussion

MDSC have emerged as major regulators of immune responses in cancer and other pathological conditions (1, 33, 34). One of the mechanisms for immunosuppression employed by MDSC in the tumor microenvironment is extracellular production of ROS (Fig. 5*A*) (19). ROS generation in MDSC is mainly due to the activity of NOX2 that oxidizes NADPH to NADP+ and then transports the electron to the extracellular side, where O_2 traps it and converts it into O_2^-. O_2^- reacts with water on the extracellular medium, producing hydrogen peroxide (H_2O_2). ROS then react with the TCR complex, abolishing the antigen presentation (1, 35). However, to sustain the ROS production in MDSC, the extrusion of protons by H_v1 is needed to counteract the cytosolic acidification and membrane depolarization caused by the NOX2 activity (26). Thus, blockade of Hv1 is a pivotal step in the suppression mechanism, as depicted in Fig. 5*B*. Overall, in this work, we have shown that H_v1 is functionally expressed in MDSC and exhibits the canonical biophysical features of this channel.

Two salient observations are noteworthy: 1) The amplitude of macroscopic proton currents recorded are ∼100 pA larger than previously reported for mouse neutrophils (24), and 2) expression of H_v1 kept increasing during a 4-d timeframe. Even though our data suggest that if the expression curve were extended to more days in myeloid differentiation stages H_v1 expression might continue to increase, an important caveat with such a large macroscopic proton current is that proton depletion during stimulation becomes significant and underestimates channel density when using standard protocols (36, 38). On the other hand, in vitro MDSC differentiation studies have demonstrated that if cells are cultured for a long time in the presence of GM-CSF they can differentiate into macrophages or dendritic cells (39–42). Macroscopic proton currents were observed at ΔpH 1 by the whole-cell patch-clamp technique in dendritic cells. The current amplitude of these recordings reached 2 nA of amplitude (43). As we found by flow cytometry, the later stages of differentiation for MDSC keep increasing H_v1 expression; our results and those obtained by Szteyn et al. (43) support the idea that myeloid cells elicit higher H_v1 expression at the latest stages of differentiation.

Redox mechanisms are frequently associated with cancer-related processes. However, as cancer development has many faces, understanding the underlying mechanism between ROS and the MDSC differentiation is still a most formidable challenge. The sustained production of ROS in MDSC is vital for maintaining immunosuppressive activity in the tumoral microenvironment (2, 44). MDSC from mice and humans release ROS to suppress T cell proliferation (16, 45, 46). The H_2O_2, formed from MDSC, decreases T cell CD3ζ expression, which restricts the activating ability of T cells (47) and lowers the expression of interferon-γ (16). It has also been shown that MDSC accumulated in tumor-bearing hosts contain high levels of ROS and peroxynitrite, which could modify T cell receptor and CD8 molecules (20).

ROS production in MDSC is not only essential to maintain their immunosuppressive properties; it also seems to be crucial to preserve their undifferentiated state (16, 48, 49). Some in vitro experiments have demonstrated that myeloid cell differentiation can be inhibited by increasing endogenous H_2O_2 (48). Nevertheless, in the absence of NOX2 activity, MDSC differentiate into both macrophage and dendritic cells (16). Therefore, both the redox state's production and maintenance seem essential to allow MDSC to fulfill their tumor defense

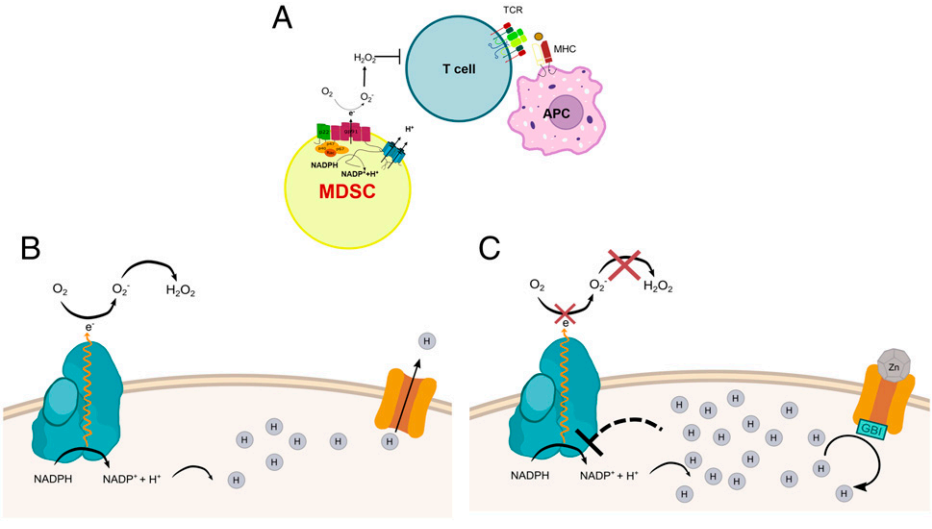

Fig. 5. H_v1 channel is responsible for ROS-mediated immunosuppression mechanism. (*A*) Modulation of ROS production by functional coupling of NOX2 and H_v1. The proliferation and response of the immune system was stimulated by the antigen presenting cells (APC) via the MHC and the TCR. When the response needs to be decreased, the MDSC produces immunosuppression in many ways, one of the main ones being ROS production by NOX2. (*B*) The normal mechanism for sustained ROS production, NOX2 oxidizes NADPH to NADP+ producing intracellular H+, the electron displaced ultimately forms H2O2 on the extracellular side and the action of Hv1 compensates for the accumulation of H+. (*C*) When Either Zn^{2+} blocks H_v1 on the extracellular side or ClGBI by the intracellular side, the accumulation of protons and consequent lowering of pH inhibits the action of NOX2, which in turn reduces the production of ROS.

function in cancer. Moreover, the modulation of H_v1 activity through the use of known inhibitors, Zn^{2+} as a nonspecific inhibitor that binds on the extracellular side of the channel (31) and ClGBI as a specific inhibitor that binds to the intracellular side (32), showed a significant reduction of MDSC-mediated cell proliferation suppression. We hypothesize that the accumulation of protons due to H_v1 inhibition with its consequent pH decrease inhibits the NOX2-mediated ROS production (Fig. 5*C*), reducing the suppressive action of MDSC. Furthermore, inhibition of H_v1 for 2 h shows a reduction of the ROS-production capabilities in MDSC (*SI Appendix*, Fig. S11*A*), and this effect remains even after 24 h of inhibitor removal (*SI Appendix*, Fig. S11*B*). The simplest way to explain the persistence of this change in the treated cells is a decrease in the viability of MDSC induced by intracellular acidification as a consequence of H_v1 channel inhibition. However, this might not be the only explanation. The 2-h incubation with inhibitors seems to be enough to trigger a phenotype change (*SI Appendix*, Fig. S12). The surface markers profile shifts when the MDSC are preincubated, whereas the presence of H_v1 remains intact (*SI Appendix*, Fig. S13), suggesting that intracellular acidification could also inhibit NOX2 function, modifying the MDSC redox state that triggers a phenotype change. Corzo et al. demonstrated that a deficiency of NOX2 activity reduces the immunosuppressive capabilities of MDSC and stimulates differentiation to dendritic cells and macrophages (16). Our data suggest that the phenotype shift occurs in the ratio of the two subpopulations that constitute the MDSC, reducing the highly suppressive MO-MDSC and increasing the moderately suppressive PMN-MDSC, in concordance with our T cell proliferation results (Fig. 4). However, further investigation needs to be performed to test this hypothesis.

H_v1 pharmacological inhibition represents an attractive and interesting approach for targeting immunosuppression in the tumoral microenvironment. From the perspective of the tumor cells, the blockage of proton extrusion through H_v1 leads to a decrease of invasiveness and migratory properties in vitro and in vivo tumor growth reduction in the human breast, glioma, and colorectal cancer cell lines (50–53). In addition, H_v1 inhibition is associated with reducing the acidification in the extracellular milieu, another critical element of T cell dysfunction in the tumoral microenvironment (54–57). Furthermore, the presence of H_v1 in some tumoral cell lines seems to be linked to their invasive capacity (58). On the other hand, from the perspective of protumoral cells such as MDSC, we demonstrate that inhibition of H_v1 induces a modulation of their immunosuppressive activity. These results strengthen the hypothesis that the pharmacological inhibition of H_v1 channel could be an excellent cancer therapy, which could be enhanced by combining it with other emerging cancer immunotherapies.

Materials and Methods

Bone Marrow-Derived Culture and MDSC Obtention. Healthy 2-mo-old C57BL/6 mice were purchased from the Bioterium of the Universidad de Valparaíso and euthanized according to the regulations of the University Animal Care Committee. Lower extremities were harvested, and the bone marrow was extracted by medium perfusion. Cells were centrifuged at 290 × *g* for 4 min and then incubated in 3 mL of ACK lysing Buffer (Thermo Fisher Scientific). The lysing buffer was rinsed with culture medium and centrifuged, and the pellet was resuspended and passed through a cell strainer of 40 μm. Cells were cultured in RPMI medium (Thermo Fisher Scientific) with 10% bovine fetal serum (Thermo Fisher Scientific), 20 μM 2-mercaptoethanol, supplemented with 0.04 μg/mL of GM-CSF (Thermo Fisher Scientific), and 1,200 units/mL of penicillin, 1,000 μg/mL of streptomycin sulfate, and 2.9 mg/mL of glutamine (Thermo Fisher Scientific). The cells were cultured at a density of 0.25×10^6 cells per mL for 4 d to allow differentiation to MDSC. On the fourth day, the cells were detached from the dish by 2.9 mM ethylenediaminetetraacetic acid (EDTA) (Invitrogen) in phosphate-buffered saline (PBS; Thermo Fisher Scientific) then resuspended in PBS and kept on ice through the full experiment.

Western Blot. Total proteins obtained from cell lysates were separated by 12% sodium dodecyl sulfate polyacrylamide gel electrophoresis (SDS-PAGE) and blotted on polyvinylidene fluoride membranes. Membranes were blocked with 5% nonfat milk in Tris-buffered saline with Tween 20 (TBS-T). A rabbit anti-mouse polyclonal H_v1 primary antibody (1:50; Invitrogen) was incubated overnight at 4 °C in TBS-T 3% BSA. After primary antibody incubation, membrane was washed and then incubated with the secondary antibody donkey anti-rabbit IgG (H+L)/HRP (Jackson ImmunoResearch, Inc.) diluted 1:10.000 for 1 h at room temperature in TBS-T 3% BSA and then washed three times. Chemiluminescence detection was performed using Immun-Star AP Chemiluminescence Kit (Bio-Rad) and images captured with a transilluminator.

Flow Cytometry.

Expression markers. On the fourth day of incubation, culture cells were recovered and incubated with Fc-blocker (Invitrogen) for 20 min with constant agitation followed by incubation with a 1:1,000 anti-mouse-CD11b/PerCP-Cy5.5 (eBiosciences), 1:1,000 anti-mouse-Gr-1/PE (eBiosciences), 1:1,000 FVS-660 (Invitrogen) and 1:50 rabbit-anti-mouse-H_v1 (Santa Cruz Biotechnology). Cells were incubated at room temperature with constant movement and protected from light for 20 min then washed and incubated with 1:100 donkey-anti-rabbit/FITC (Invitrogen) for 20 min at room temperature and protected from light. Finally, cells were washed and resuspended in 500 μL of PBS and run through the flow cytometer (BD Accuri C6) until at least 100,000 events were recorded.

Expression kinetics. Bone marrow cells were cultured at different times in the presence of GM-CSF. The evaluated time points were 0, 24, 48, 72, 96, 120, 144, and 168 h of incubation. At these stages, the expression kinetics of H_v1 protein and the phenotype changes of cultured cells during the differentiation protocol were assessed. At every stage, the cells were incubated with mouse Fc-Blocker (Invitrogen), anti-mouse-CD11b/PerCP-Cy5.5, anti-mouse-Gr-1/PE, anti-mouse-F4/80/APC (eBiosciences), and rabbit-anti-mouse-H_v1, followed by donkey anti-rabbit/FITC. Each stage of differentiation was then run through the cytometer until at least 100,000 events were recorded.

Electrophysiology. The whole-cell patch-clamp technique was employed to measure macroscopic H^+ currents on cultured MDSC (96 h cultured in the presence of GM-CSF). Measurements were performed at room temperature. The bath solution was grounded using a KCl 3 M agar bridge. Borosilicate glass pipettes (1B150F-4; World Precision Instruments) were pulled using a P-97 horizontal pipette puller (Sutter Instruments Co.) and then polished with a microforge (MF-830; Narishige International, USA, Inc.), obtaining tip resistances of 1 to 5 MΩ in the bath solution. Glass pipettes were mounted in an electric micromanipulator PSC-6000 (Burleigh). MDSC proton currents were acquired with an AxoPatch 200B amplifier (Axon Instruments) and filtered at 10 kHz with an eight-pole Bessel low-pass filter. The analog signal was sampled at 100 kHz and digitalized by Digidata 1440A (Axon Instruments). No access resistance compensation was performed. Experiments were performed using the Clampex 10.7 software (Axon Instruments). The recording solution was adjusted to pH 7.5 and contained 100 mM Hepes buffer, 2 mM $MgCl_2$, 1 mM ethylene glycol bis(β-aminoethyl ether)-*N*,*N*,*N*′,*N*′-tetraacetic acid (EGTA), 30 mM tetraethylammonium hydroxide (TEAOH), and 160 mM *N*-methyl-D-glucamine (NMDG)-methanesulfonate. Recording solutions at pH 6.5 and 5.5 contained 100 mM MES (2-(*N*-morpholino)ethanesulfonic acid) buffer, 2 mM $MgCl_2$, 1 mM EGTA, 30 mM TEAOH, and 160 mM NMDG-methanesulfonate. Solution osmolarity was measured and adjusted to 300 mOsm with glucose. Proton ΔpH dependency was studied by eliciting the proton currents using a variable duration pulse protocol from −90 mV to 130 mV in 20-mV steps. The duration of the voltage pulses was optimized to avoid proton depletion. The current activation data were fitted using a Boltzmann equation for a two-state closed-open model:

$$\frac{G}{G_{max}} = \frac{1}{1 + exp^{\frac{[-z\delta(V_m - V_{0.5})]}{RT}}}, \quad [1]$$

where G/G_{max} is the normalized conductance, $z\delta$ is the apparent gating charge, V_m is the applied membrane potential, $V_{0.5}$ is the half activation potential, R is the ideal gas constant, and T is the absolute temperature (295 K).

To assess H^+ selectivity of the H_v1 channel, the reversal potential (E_r) was calculated using a fast ramp pulse protocol (59–61) at different ΔpH conditions (*SI Appendix*, Fig. S5). This protocol consisted of a series of variable duration prepulses from −90 to 130 mV in 10-mV increments. At the end of each prepulse, the membrane potential was taken to 130 mV, from where a fast potential ramp was applied to −140 mV. The voltage at which current traces intersect each other corresponds to the experimental E_r. To reliably evaluate the overlap of current traces, we determined the time when the variance of current traces produced by the ramp potential was minimal (*SI Appendix*, Fig. S5*B*). This value was then compared to the proton equilibrium potential (E_{H^+}) predicted by the Nernst equation:

$$E_{H^+} = \frac{RT}{zF} \ln \frac{[H^+]_{out}}{[H^+]_{in}}, \quad [2]$$

where z is the ion valence, $[H^+]$ the proton concentration, F is Faraday's constant, R is the ideal gas constant, and T is the absolute temperature (295 K). For further explanation of the fast ramp protocol see *SI Appendix*.

For proton current inhibition assays, recording solutions containing 10 μM $ZnCl_2$ or 100 μM ClGBI were perfused into the recording chamber. A 130-mV depolarization generated a current trace before and after perfusion with the inhibitor.

ROS Assays. To assess the functional coupling between the H_v1 channel and NOX2, MDSC were incubated with the ROS-sensitive probe H_2DCFDA (Invitrogen) at 2.5 μM for 10 min on ice and protected from light. MDSC were stimulated by the addition of 100 nM of PMA (Invitrogen) and immediately the fluorescence emitted by the probe was recorded for 10 min by flow cytometry. Different assays were performed in the presence and absence of H_v1 blockers (1 mM $ZnCl_2$ or 200 μM ClGBI). To estimate the ROS production, the data were fitted to a curve in the form

$$y = \frac{a * x}{(b + x)}, \quad [3]$$

where a and b are free variables for the optimization and y corresponds to fluorescence intensity and x to time, in what is referred to as a Michaelis–Menten-like curve using Python. To have some quantity to compare between the assays, the area below the curve was calculated by integrating the curve during the whole 10 min of the experiment. This amount represents the total ROS production in each condition in triplicate. For the control experiments, the Hv1 inhibitors were rinsed using 0.5 mM EDTA in PBS.

Proliferation Assays. T cells were obtained from healthy C57BL/6 mice, cultured in RPMI medium, and incubated in the presence of CFSE probe (Invitrogen). This fluorophore enters the cells and then makes covalent complexes with cytoskeleton proteins. When the cells go to mitosis, the amount of CFSE present in them is divided between the resulting cells, causing a decrease in fluorescence intensity with each passing generation (*SI Appendix*, Fig. S7) (62). The T cells were then cocultured with MDSC (*SI Appendix*, Fig. S8). The mitogen ConA (eBiosciences) was added at 2 μg/mL concentration to the cultures to promote proliferation. The fluorescence intensity of the cultures was assessed by the FL1 range in the BD Accuri C6 flow cytometer. The same experiment was later performed incubating the MDSC cultures with the H_v1 inhibitors and their corresponding vehicles (dimethyl sulfoxide [DMSO] for ClGBI and PBS for $ZnCl_2$) for 2, 12, and 24 h. After this preincubation, the cells were detached from the dishes and washed thoroughly with 0.5 mM EDTA in PBS to avoid carrying the inhibitors to the T cell cultures. A prior control of T cell viability was performed (*SI Appendix*, Fig. S9); in it a culture of T cells was extracted and diluted in 450 μL of PBS and then was added 50 μL of ethanol 70% (Et-OH, positive control for cell lethality), 50 μL of $ZnCl_2$ 1 mM, 50 μL of $ZnCl_2$ 0.5 mM, or 50 μL of PBS as a control. The T cells reached less than 50% viability whenever $ZnCl_2$ was added to the culture, similar to the results obtained by other authors when inhibiting Hv1 on leukemic cells (57).

Statistics. The data transfer and processing were performed by the software FlowJo, the same software used to calculate the fluorescence compensation for the multiple channel experiments. The data of MFI was obtained from FlowJo and exported to GraphPad's Prism 6 software for statistical analysis through one-way ANOVA, Kruskal–Wallis nonparametric, and nonparametric Student *t* tests.

Data Availability. All study data are included in the article and/or *SI Appendix*.

ACKNOWLEDGMENTS. We thank Donna Loyle, MS, Communications Manager at LIMR, for copyediting this manuscript, Dr. Natalia Saez from Traduc Ltd. for proofreading services, and Dr. Luis Cuello and Rafael Paredes for support and hard work. This work was supported by Comisión Nacional de Investigación Científica y Tecnológica (CONICYT)/Programa Formación de Capital Humano Avanzado/Doctorado Nacional/2019-21200754 to C.C., 2019-21200727 to J.J.A.-A., 2018-21191239 to A.P., 2017-21171141 to M.F., 2017-21170395 to E.M.C., Fondecyt 1180464 - 1220327 to C.G., 1190203 to R.L., 1161672 to A.N., 1180987 to J.G., P.A.I. grant 77170045 to J.G., and UJED-CONACYT-CB-2015-01-259091 to A.L.-R. The Centro Interdisciplinario de Neurociencia de Valparaiso (CINV) and the NNBP are funded by the ANID-Millennium Science Initiative Program projects IACE210014 and NCN2021_021. This work was also supported by The Lankenau Institute for Medical Research Charitable Foundation, National Heart, Lung, and Blood Institute (grants HL47678, HL138103, and HL152201), NIH National Institute of General Medical Sciences grant 109762, and National Heart, Lung and Blood Institute grant 131461 to H.P.L.

Author affiliations: [a]Millenium Institute Centro Interdisciplinario de Neurociencia de Valparaíso, Facultad de Ciencias, Universidad de Valparaíso, Valparaíso 236 0102, Chile; [b]Millenium Nucleus in NanoBioPhysics (NNBP), Universidad de Valparaíso, Valparaíso 236 0102, Chile; [c]Departamento de Biología, Facultad de Ciencias, Universidad de Chile, Santiago 7800003, Chile; [d]Cardiovascular Research, Lankenau Institute for Medical Research, Wynnewood, PA 19096; [e]Department of Physiology & Biophysics, University of Miami, Coral Gables, FL 33101; and [f]Facultad de Ciencias Químicas, Universidad Juárez del Estado de Durango, Durango 34000, México

Author contributions: J.J.A.-A., C.C., A.F., E.M.C., A.P., and C.G. designed research; J.J.A.-A., C.C., J.P.V., R.G.-B., A.P.-P., A.F., M.F., E.M.C., and C.G. performed research; A.N. and C.G. contributed new reagents/analytic tools; J.J.A.-A., C.C., J.P.V., R.G.-B., A.P.-P., A.F., M.F., E.M.C., O.A., and C.G. analyzed data; and J.J.A.-A., C.C., M.F., A.N., O.A., J.G., H.B.-M., H.P.L., A.L.-R., R.L., and C.G. wrote the paper.

1. D. I. Gabrilovich, Myeloid-derived suppressor cells. *Cancer Immunol. Res.* **5**, 3–8 (2017).
2. P. Serafini, Myeloid derived suppressor cells in physiological and pathological conditions: The good, the bad, and the ugly. *Immunol. Res.* **57**, 172–184 (2013).
3. V. Bronte *et al.*, Recommendations for myeloid-derived suppressor cell nomenclature and characterization standards. *Nat. Commun.* **7**, 12150 (2016).
4. V. Bronte *et al.*, Unopposed production of granulocyte-macrophage colony-stimulating factor by tumors inhibits CD8+ T cell responses by dysregulating antigen-presenting cell maturation. *J. Immunol.* **162**, 5728–5737 (1999).
5. K. Movahedi *et al.*, Identification of discrete tumor-induced myeloid-derived suppressor cell subpopulations with distinct T cell-suppressive activity. *Blood* **111**, 4233–4244 (2008).
6. E. Peranzoni *et al.*, Myeloid-derived suppressor cell heterogeneity and subset definition. *Curr. Opin. Immunol.* **22**, 238–244 (2010).
7. F. De Sanctis, V. Bronte, S. Ugel, Tumor-induced myeloid-derived suppressor cells. *Microbiol. Spectr.* **4**, 10.1128/microbiolspec.MCHD-0016-2015 (2016).
8. A. Kotsakis *et al.*, Myeloid-derived suppressor cell measurements in fresh and cryopreserved blood samples. *J. Immunol. Methods* **381**, 14–22 (2012).
9. T. F. Greten, M. P. Manns, F. Korangy, Myeloid derived suppressor cells in human diseases. *Int. Immunopharmacol.* **11**, 802–807 (2011).
10. A. M. Bruger *et al.*, How to measure the immunosuppressive activity of MDSC: Assays, problems and potential solutions. *Cancer Immunol. Immunother.* **68**, 631–644 (2019).
11. I. Marigo, L. Dolcetti, P. Serafini, P. Zanovello, V. Bronte, Tumor-induced tolerance and immune suppression by myeloid derived suppressor cells. *Immunol. Rev.* **222**, 162–179 (2008).
12. A. Fernández, A. Pupo, K. Mena-Ulecia, C. Gonzalez, Pharmacological modulation of proton channel Hv1 in cancer therapy: Future perspectives. *Mol. Pharmacol.* **90**, 385–402 (2016).
13. M. K. Srivastava, P. Sinha, V. K. Clements, P. Rodriguez, S. Ostrand-Rosenberg, Myeloid-derived suppressor cells inhibit T-cell activation by depleting cystine and cysteine. *Cancer Res.* **70**, 68–77 (2010).
14. P. C. Rodriguez *et al.*, Arginase I production in the tumor microenvironment by mature myeloid cells inhibits T-cell receptor expression and antigen-specific T-cell responses. *Cancer Res.* **64**, 5839–5849 (2004).
15. C. A. Corzo *et al.*, HIF-1α regulates function and differentiation of myeloid-derived suppressor cells in the tumor microenvironment. *J. Exp. Med.* **207**, 2439–2453 (2010).
16. C. A. Corzo *et al.*, Mechanism regulating reactive oxygen species in tumor-induced myeloid-derived suppressor cells. *J. Immunol.* **182**, 5693–5701 (2009).
17. P. L. Raber *et al.*, Subpopulations of myeloid-derived suppressor cells impair T cell responses through independent nitric oxide-related pathways. *Int. J. Cancer* **134**, 2853–2864 (2014).
18. O. P. Joffre, E. Segura, A. Savina, S. Amigorena, Cross-presentation by dendritic cells. *Nat. Rev. Immunol.* **12**, 557–569 (2012).
19. T. A. Chan *et al.*, Development of tumor mutation burden as an immunotherapy biomarker: Utility for the oncology clinic. *Ann. Oncol.* **30**, 44–56 (2019).

20. S. Nagaraj *et al.*, Altered recognition of antigen is a mechanism of CD8+ T cell tolerance in cancer. *Nat. Med.* **13**, 828–835 (2007).
21. T. E. DeCoursey, V. V. Cherny, A. G. DeCoursey, W. Xu, L. L. Thomas, Interactions between NADPH oxidase-related proton and electron currents in human eosinophils. *J. Physiol.* **535**, 767–781 (2001).
22. D. Morgan, V. V. Cherny, R. Murphy, B. Z. Katz, T. E. DeCoursey, The pH dependence of NADPH oxidase in human eosinophils. *J. Physiol.* **569**, 419–431 (2005).
23. T. E. DeCoursey, D. Morgan, V. V. Cherny, The voltage dependence of NADPH oxidase reveals why phagocytes need proton channels. *Nature* **422**, 531–534 (2003).
24. I. S. Ramsey, E. Ruchti, J. S. Kaczmarek, D. E. Clapham, Hv1 proton channels are required for high-level NADPH oxidase-dependent superoxide production during the phagocyte respiratory burst. *Proc. Natl. Acad. Sci. U.S.A.* **106**, 7642–7647 (2009).
25. Y. Okochi, M. Sasaki, H. Iwasaki, Y. Okamura, Voltage-gated proton channel is expressed on phagosomes. *Biochem. Biophys. Res. Commun.* **382**, 274–279 (2009).
26. T. E. DeCoursey. Voltage gated proton channels find their dream job managing the respiratory burst in phagocytes. *Physiology (Bethesda)* **42**, 115–125 (2010).
27. I. S. Ramsey, M. M. Moran, J. A. Chong, D. E. Clapham, A voltage-gated proton-selective channel lacking the pore domain. *Nature* **440**, 1213–1216 (2006).
28. M. Sasaki, M. Takagi, Y. Okamura, A voltage sensor-domain protein is a voltage-gated proton channel. *Science* **312**, 589–592 (2006).
29. V. V. Cherny, V. S. Markin, T. E. DeCoursey, The voltage-activated hydrogen ion conductance in rat alveolar epithelial cells is determined by the pH gradient. *J. Gen. Physiol.* **105**, 861–896 (1995).
30. V. V. Cherny, R. Murphy, V. Sokolov, R. A. Levis, T. E. DeCoursey, Properties of single voltage-gated proton channels in human eosinophils estimated by noise analysis and by direct measurement. *J. Gen. Physiol.* **121**, 615–628 (2003).
31. F. Qiu *et al.*, Molecular mechanism of Zn^{2+} inhibition of a voltage-gated proton channel. *Proc. Natl. Acad. Sci. U.S.A.* **113**, E5962–E5971 (2016).
32. L. Hong, I. H. Kim, F. Tombola, Molecular determinants of Hv1 proton channel inhibition by guanidine derivatives. *Proc. Natl. Acad. Sci. U.S.A.* **111**, 9971–9976 (2014).
33. C. Goh, S. Narayanan, Y. S. Hahn, Myeloid-derived suppressor cells: The dark knight or the joker in viral infections? *Immunol. Rev.* **255**, 210–221 (2013).
34. V. Kumar, S. Patel, E. Tcyganov, D. I. Gabrilovich, The nature of myeloid-derived suppressor cells in the tumor microenvironment. *Trends Immunol.* **37**, 208–220 (2016).
35. A. Savina *et al.*, NOX2 controls phagosomal pH to regulate antigen processing during crosspresentation by dendritic cells. *Cell* **126**, 205–218 (2006).
36. V. De-la-Rosa, E. Suárez-Delgado, G. E. Rangel-Yescas, L. D. Islas, Currents through Hv1 channels deplete protons in their vicinity. *J. Gen. Physiol.* **147**, 127–136 (2016).
37. T. E. DeCoursey, Voltage and pH sensing by the voltage-gated proton channel, H_v1. *J. R. Soc. Interface* **15**, 20180108 (2018).
38. T. E. DeCoursey, V. V. Cherny, Effects of buffer concentration on voltage-gated H+ currents: Does diffusion limit the conductance? *Biophys. J.* **71**, 182–193 (1996).
39. J.-I. Youn, M. Collazo, I. N. Shalova, S. K. Biswas, D. I. Gabrilovich, Characterization of the nature of granulocytic myeloid-derived suppressor cells in tumor-bearing mice. *J. Leukoc. Biol.* **91**, 167–181 (2012).
40. T. Condamine, *et al.*, Lectin-type oxidized LDL receptor-1 distinguishes population of human polymorphonuclear myeloid-derived suppressor cells in cancer patients. *Sci. Immunol.* **1**, aaf8943 (2016).
41. M. F. Tavazoie *et al.*, LXR/ApoE activation restricts innate immune suppression in cancer. *Cell* **172**, 825–840.e18 (2018).
42. M. Gato *et al.*, Drafting the proteome landscape of myeloid-derived suppressor cells. *Proteomics* **16**, 367–378 (2016).
43. K. Szteyn, W. Yang, E. Schmid, F. Lang, E. Shumilina, Lipopolysaccharide-sensitive H+ current in dendritic cells. *Am. J. Physiol. Cell Physiol.* **303**, C204–C212 (2012).
44. L. Wang *et al.*, Reactive oxygen species in immune cells: A new antitumor target. *Biomed. Pharmacother.* **133**, 110978 (2021).
45. X. Chen, M. Song, B. Zhang, Y. Zhang, Reactive oxygen species regulate T cell immune response in the tumor microenvironment. *Oxid. Med. Cell. Longev.* **2016**, 1580967 (2016).
46. H. Zhang *et al.*, Myeloid-derived suppressor cells inhibit T cell proliferation in human extranodal NK/T cell lymphoma: A novel prognostic indicator. *Cancer Immunol. Immunother.* **64**, 1587–1599 (2015).
47. J. Schmielau, O. J. Finn, Activated granulocytes and granulocyte-derived hydrogen peroxide are the underlying mechanism of suppression of t-cell function in advanced cancer patients. *Cancer Res.* **61**, 4756–4760 (2001).
48. S. Kusmartsev, D. I. Gabrilovich, Inhibition of myeloid cell differentiation in cancer: The role of reactive oxygen species. *J. Leukoc. Biol.* **74**, 186–196 (2003).
49. D. W. Beury *et al.*, Myeloid-derived suppressor cell survival and function are regulated by the transcription factor Nrf2. *J. Immunol.* **196**, 3470–3478 (2016).
50. Y. Wang *et al.*, Specific expression of the human voltage-gated proton channel Hv1 in highly metastatic breast cancer cells, promotes tumor progression and metastasis. *Biochem. Biophys. Res. Commun.* **412**, 353–359 (2011).
51. Y. Wang, S. J. Li, X. Wu, Y. Che, Q. Li, Clinicopathological and biological significance of human voltage-gated proton channel Hv1 protein overexpression in breast cancer. *J. Biol. Chem.* **287**, 13877–13888 (2012).
52. Y. Wang, S. Zhang, S. J. Li, Zn(2+) induces apoptosis in human highly metastatic SHG-44 glioma cells, through inhibiting activity of the voltage-gated proton channel Hv1. *Biochem. Biophys. Res. Commun.* **438**, 312–317 (2013).
53. Y. Wang, X. Wu, Q. Li, S. Zhang, S. J. Li, Human voltage-gated proton channel Hv1: A new potential biomarker for diagnosis and prognosis of colorectal cancer. *PLoS One* **8**, e70550 (2013).
54. F. Redegeld, A. Filippini, M. Sitkovsky, Comparative studies of the cytotoxic T lymphocyte-mediated cytotoxicity and of extracellular ATP-induced cell lysis. Different requirements in extracellular Mg^{2+} and pH. *J. Immunol.* **147**, 3638–3645 (1991).
55. L. Lugini *et al.*, Cannibalism of live lymphocytes by human metastatic but not primary melanoma cells. *Cancer Res.* **66**, 3629–3638 (2006).
56. A. Calcinotto *et al.*, Modulation of microenvironment acidity reverses anergy in human and murine tumor-infiltrating T lymphocytes. *Cancer Res.* **72**, 2746–2756 (2012).
57. A. Asuaje *et al.*, The inhibition of voltage-gated H^+ channel (HVCN1) induces acidification of leukemic Jurkat T cells promoting cell death by apoptosis. *Pflugers Arch.* **469**, 251–261 (2017).
58. D. J. Bare, V. V. Cherny, T. E. DeCoursey, A. M. Abukhdeir, D. Morgan, Expression and function of voltage gated proton channels (Hv1) in MDA-MB-231 cells. *PLoS One* **15**, e0227522 (2020).
59. E. M. Carmona *et al.*, Gating charge displacement in a monomeric voltage-gated proton (H_v1) channel. *Proc. Natl. Acad. Sci. U.S.A.* **115**, 9240–9245 (2018).
60. C. Gonzalez, H. P. Koch, B. M. Drum, H. P. Larsson, Strong cooperativity between subunits in voltage-gated proton channels. *Nat. Struct. Mol. Biol.* **17**, 51–56 (2010).
61. E. M. Carmona *et al.*, The voltage sensor is responsible for ΔpH dependence in H_v1 channels. *Proc. Natl. Acad. Sci. U.S.A.* **118**, e2025556118 (2021).
62. A. B. Lyons, C. R. Parish, Determination of lymphocyte division by flow cytometry. *J. Immunol. Methods* **171**, 131–137 (1994).